

## Chapter 16

### Controlled nanostructuring of transparent matter with temporal Airy pulses

T. Winkler<sup>\*1</sup>, B. Zielinski<sup>2</sup>, C. Sarpe<sup>2</sup>, R. Ciobotea<sup>2</sup>, A. Senftleben<sup>2</sup>, T. Baumert<sup>2</sup>

**1** Department of Physics and Astronomy, Aarhus University, 8000 Aarhus C, Denmark

**2** Institute for Physics and Cinsat, University of Kassel, 34121 Kassel, Germany

\* [winkler@phys.au.dk](mailto:winkler@phys.au.dk)

#### Abstract:

Ultrashort near-infrared femtosecond laser pulses have become the tool of choice for high-precision processing of transparent ultrawide bandgap materials, ranging from material ablation, amorphization, waveguide writing to optical data-storage. The processing precision with ultrashort laser pulses is fundamentally limited in the lateral direction by diffraction, while self-absorption and self-reflection are limiting the achievable depth. Here, we present one of the possible pathways to overcome these limits by utilizing temporal pulse shaping technology. In the following, we review and discuss the main light–matter interaction mechanisms, multi-photon and avalanche excitation, and how ultrashort and temporally shaped femtosecond laser pulses address them differently, allowing the control over the spatial carrier distribution and the subsequent material processing. We demonstrate the potential of temporal pulse shaping as a tool for controlled nanostructuring below the typical limits by discussing our in-situ and post-mortem experimental and numerical studies on the spatial distribution of laser excitation in water, high-aspect-ratio structuring of fused silica, and the optoporation of cells.

#### 1 Introduction to nanostructuring of transparent matter with temporally adapted pulses

Material processing based on ultrashort laser pulses in the near infrared has become a well-established field that has emerged over the last decades [1–3] and enables key technologies for a variety of applications ranging from micro- and nano processing of dielectric materials for photonics to medical and biological research. Based on the precision of laser ablation due to a strongly reduced heat-affected zone that is unattainable by other technologies, femtosecond-laser processing remains the tool of choice. In recent years, the limits of the processing precision have experienced significant shifts by temporal, spatial and combined pulse-shaping techniques, as demonstrated in chapters 8, 15, 33 and 38.

In contrast to spatial pulse shaping techniques, which – as the name suggests – influence the ablation characteristics by varying the incident fluence/intensity distribution (e.g. by using non-diffracting Bessel beams), temporal pulse shaping addresses the interplay of different excitation mechanisms in transparent matter to manipulate and control the ablation characteristics such as the removal-rate or enabling sub-diffraction limited ablation, while maintaining the classical Gaussian spatial beam profile and propagation properties. Over the years, temporal pulse shaping has developed from straightforward Michelson-interferometer based double-pulses with variable inter pulse delay (e.g. [4–6]) or simple stretching/chirping of pulses using gratings or prisms (e.g. [7, 8]) to the application of complex temporal and polarization forms created by liquid-crystal-display (LCD) based pulse shapers (see [9–12] and references therein). These techniques address the manipulation of the light-matter interaction on relatively short timescales and thus influence the initial step of electron plasma formation. Similarly, the creation of bursts of closely spaced pulses (nanoseconds) at high repetition rates, commonly referred to as “burst-mode”, have enabled another pathway of processing through addressing the interplay between excitation and heating with a high-throughput at relatively low costs [13–16].

In this chapter, we will demonstrate an approach to control the precision of laser processing of transparent materials: Temporally asymmetric shaped laser pulses, i.e. *temporal Airy pulses* (TAP).

In the subsequent sections, we will discuss the current understanding about why asymmetric shaped laser pulses are a perfect tool for precision processing of transparent matter. Measuring and modeling how these laser pulses interact and address the different interaction mechanisms at play in water, sapphire, and fused silica lays the foundation of our understanding which in-turn enables sophisticated applications, exemplified by our studies on single cell optoporation.

## 2 Fundamentals of energy deposition by temporally shaped femtosecond laser pulses into dielectrics

In this section, we discuss the fundamental light–matter interaction mechanisms that allow for the excitation of carriers in ultrawide bandgap dielectrics by near-infrared femtosecond laser pulses, being the first step in every ablation process: Strong field and avalanche excitation [17]. Subsequent, we discuss spatially resolved real-time measurements of the excitation of water by ultrashort femtosecond and temporal Airy pulses and compare the experimental results with numerical simulations, demonstrating the unique spatial carrier distribution that can be achieved by temporal pulse shaping.

### 2.1 Seed and heat mechanism by strong field and avalanche excitation

To enable the processing of transparent materials with femtosecond laser pulses, a sufficient amount of energy needs to be deposited by a laser pulse, causing permanent changes to the material, such as refractive index modification [18–20], amorphization of crystalline material [21, 22] or the permanent removal of such (i.e., ablation) [23, 24]. Typically, near-infrared femtosecond laser pulses of wavelengths around 800 nm are used for processing purposes. Consequentially, the photon energy of only 1.5 eV is insufficient to simply excite valence band electrons into the conduction band across the bandgap of usually around 6–12 eV, depending on the dielectric material. However, sufficiently high intensities of the laser pulse allow for the simultaneous absorption of multiple photons by valence band electrons to be promoted into the conduction band, naming it multi-photon excitation [25]. While initially the number of photons required for the multiphoton process is simply given by the ratio of the bandgap energy to the photon energy, for increasing intensity of the pump pulse, the quiver energy of the electrons increase the apparent bandgap energy of the material (i.e. the Ponderomotive energy shift) [17, 25]. Thus, the multi-photon process can change the order of nonlinearity during the temporal profile of an intense laser pulse. At an even higher intensity, the chances of tunnel excitation/ionization increase substantially [25]. Here, valence band electrons tunnel across the gap due to the tilted potential following the strong electric field of the laser pulse.

The electrons promoted to the conduction band via strong-field excitation act as a seed for a secondary excitation channel: avalanche excitation [17]. The quasi-free electrons in the conduction band can absorb single photons from the near infrared laser pulse via inverse-Bremsstrahlung absorption, gaining kinetic energy. Once the kinetic energy of the conduction band electron exceeds the bandgap energy of the material, another valence band electron can be promoted to the conduction band via impact excitation, leaving two electrons close to the bottom of the conduction band, ready to repeat the process. Thus, impact excitation can lead to a self-reinforcing multiplication of the conduction band electron density, giving the process its well-known name.

For a more detailed review of the excitation pathways in dielectric materials, we refer to Balling and Schou [17] and the references therein.

The change in the electron density as a function of time  $N_e(t)$  is typically described by a rate equation in the form of [17]:

$$\frac{\partial N_e(t)}{\partial t} = \eta_{SFE}(t) + \eta_{AE}(t) \quad 1$$

where the first part describes the rate of carrier excitation by strong-field excitation (SFE) whereas the second term describes the contribution by avalanche excitation.

While there exists a manifold of theoretical descriptions of both contributions, the Keldysh formalism [25, 26] and the multiple rate equation model [27, 28] are currently the most commonly used models for strong-field and avalanche excitation, respectively. However, recently, a novel and powerful approach to model the avalanche excitation process – a dynamical rate equation model – was introduced by Déziel *et al* [29].

In order to draw a simple picture, we limit ourselves to a phenomenological description of the processes via the following rate equation:

$$\frac{\partial N_e(t)}{\partial t} \propto \frac{N_e}{N_{eMax}} (\sigma_n I^n(t) + \alpha I(t) N_e(t)) \quad 2$$

With  $\sigma_n$ , the n-th order multi-photon excitation coefficient and  $\alpha$ , the avalanche excitation coefficient.  $I(t)$  is the time-dependent intensity of the exciting laser pulse. As the excitation of free carriers will diminish the amount of available valence band electrons  $N_e$ , a stagnation factor  $N_e/N_{e_{Max}}$  – given as the ratio of current to maximum available electrons for excitation ( $N_{e_{Max}}$ ) – is introduced.

The limits of Eq. (2) become immediately apparent, exemplified in the inability to capture changing orders of the multiphoton process due to the bandgap increase by Ponderomotive energy shifts, or by increasing probability of tunneling excitation. Another limitation of Eq. (2) is the description of avalanche excitation, as here the intensity interacts with the current electron density. However, after each free-carrier-absorption event, the electron must scatter for momentum conservation [17]. Thus, the actual impact excitation process is delayed with respect to the exciting laser pulse. While the proper description in keeping track of the how many conduction electrons have how much kinetic energy is well established by using a multiple or dynamical rate equation model as mentioned above, we make use of an approach first introduced by Vogel and coworkers [30]. By introducing a retardation-time:

$$t_{ret} = t - n' \cdot \tau \quad 3$$

with  $n'$  the number of photons required to obtain sufficient energy for impact excitation, being approx. 1.5x the bandgap energy [31] and the time between scattering events  $\tau$  (i.e. the electron scattering time), we rewrite Eq. (2) to be:

$$\frac{\partial N_e(t)}{\partial t} \propto \frac{N_e}{N_{e_{Max}}} (\sigma_n I^n(t) + \alpha I(t) N_e(t_{ret})) \quad 4$$

Thus, the light field at time  $t$  only creates avalanche excitation with conduction band electrons present at time the  $t_{ret}$ .

Although Eq. (4) is a strong simplification of the complex excitation processes, we will demonstrate in the subsequent sections, that this description of the excitation in the moderate excitation regime can capture the physics involved in the interaction of temporally asymmetric shaped femtosecond laser pulses. From Eq. (4) it already becomes clear that depending on the duration or the temporal shape of an incident exciting laser pulse multiphoton and avalanche excitation are addressed very differently.

This aspect can be best illustrated by comparing the time-dependent conduction band carrier density created by two temporal Airy pulse of opposite temporal shape, as they have the same energy and peak intensity – thus allowing for a fair comparison.

While there exist many ways to temporally shape laser pulses, spectral phase modulation remains the only way to precisely shape the temporal profile of ultrashort laser pulses [32]. Here, different spectral components of femtosecond laser pulse are delayed with respect to each other, i.e. by applying a spectral phase modulation. Typically described in a Taylor expansion around the central angular frequency of the laser pulse, the second order phase term will lead to a group delay dispersion (GDD), i.e. a classical chirp of the pulse, while the third order term (“third order dispersion”) causes the creation of asymmetric temporal Airy pulses, whose envelope is described by an Airy function with an exponential decay [33]. A complete mathematical description of spectral pulse shaping with an in-depth discussion can be found in [34].

Figure 1 shows the intensity profile of two temporal Airy pulses created with a third order dispersion term of  $+6 \times 10^5 \text{ fs}^3$  (red line) and  $-6 \times 10^5 \text{ fs}^3$  (blue line). The asymmetric pulses consist of a main pulse with a subsequent train of pulses with ever decreasing intensity and sub-pulse separation. The sign of the phase simply flips the temporal profile, making the temporal airy pulse with a negative phase start with the least intense sub pulse.

Figure 1 also demonstrates how these two temporal Airy pulses with equal pulse energy and peak intensities will create a significantly different carrier density in a dielectric material. We calculated the time dependent conduction band electron density using Eq. (4) with details given in [35].

Using the positive TAP pulse, we observe a sharp increase in carrier density at the beginning of the pulse which is mainly produced by SFE (red dashed labeled  $N_e^+(\text{SFE})$  in Fig. 1) and that each of the pulses of the train further increases the carrier density by AI reaching the maximum carrier density at the end of the pulse. The negative TAP pulse, on the other hand, creates a significantly smaller final carrier density, despite the equal energy and

peak intensity. It does, however, create the same number of free carriers via SFE (blue dashed line  $N_e^-(\text{SFE})$ ), but only at the very end of the main pulse, meaning only a small fraction of avalanche excitation can take place. In this example, the train of smaller pulses of the negative TAP is not absorbed at all and the final sub-pulse acts similar to an ultrashort laser pulse.

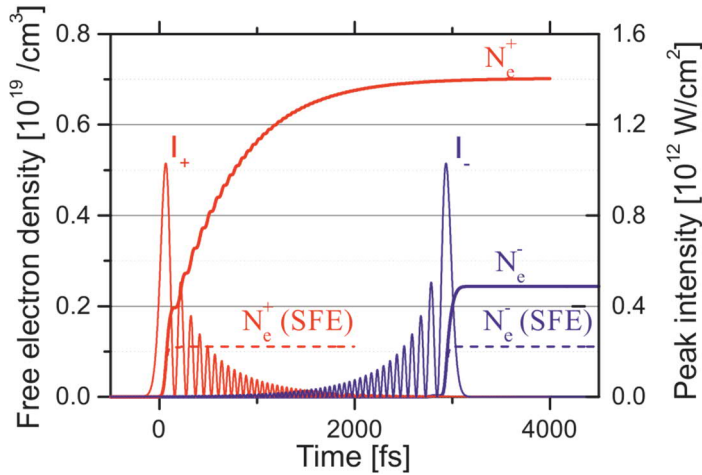


Figure 1 - Calculated time-dependent conduction band electron density  $N_e$  taking multiphoton and avalanche ionization into account (solid lines) for positive (red curves, index +) and negative (blue curves, index -) TAP pulses with a third-order dispersion coefficient of  $\pm 600000 \text{ fs}^3$ . The contribution by pure multiphoton ionization is indicated as well (dashed lines  $N_e^\pm(\text{SFE})$ ). The corresponding transient intensities of the modulated pulses are also presented ( $I_+, I_-$ ). The curves for negative shaped pulses are offset by 3 ps in time for better visualization. Reproduced from [35]. © IOP Publishing and Deutsche Physikalische Gesellschaft. Reproduced by permission of IOP Publishing. All rights reserved.

The slow rise in carrier density over the course of the temporal profile of the positive TAP pulse delivers significant advantages over Gaussian-shape ultrashort laser pulses where the carrier density rises very fast at the much higher peak intensities. We will explore and discuss the superiority of positive TAP pulses in the excitation and ablation of transparent laser pulses based in the subsequent chapters.

## 2.2 Real-time spatially resolved measurements of energy deposition in water

With the excitation of any dielectric material, i.e. the promotion of valence band electrons to the conduction band, a change in the optical properties is induced. While usually being transparent to visible light due to a large bandgap energy, the creation of a high charge carrier density will provide the dielectric material with metallic properties. It is also the first step in the processing of materials, as the charge carriers are the mediators in the energy transfer from the laser pulse to the material that can cause permanent changes like e.g. the formation of defects, ablation or (cavitation) bubble formation in the case of water. Consequentially, the density of the charge carriers and their spatial distribution in the interaction area of the laser pulse are decisive for the result of any modification process.

### 2.2.1 Optical properties of excited dielectrics

To create the fundamental understanding of laser energy deposition with TAP pulses and to directly observe the impact of temporal pulse shaping on the spatial properties of the laser excitation, we performed time and spatially resolved pump probe measurement on liquid water. The choice of liquid water as the sample system is based on three aspects: First, water can be treated as an amorphous semiconductor and shares the main excitation pathways and optical properties with its solid cousins like e.g. sapphire; second, using liquid water makes it easy to have an unlimited sample supply and to provide a fresh sample volume for each laser pulse; lastly, studying the excitation of water is of high interest for any biological or medical related applications, as we will discuss in section 3.

The optical properties of an excited dielectric material are typically well captured by the Drude-model, providing the complex dielectric function for a material with a magnetic permeability of 1 [36]:

$$\varepsilon(\omega) = \varepsilon_b - \frac{\omega_{pl}^2}{\omega^2 + i\omega\tau^{-1}}, \quad 5$$

where  $\varepsilon_b$  is the dielectric constant of the unexcited material, where the second part describes the contribution by the quasi-free electrons with  $\tau$  the electron scattering time,  $\omega$  the angular frequency of the incident light field and  $\omega_{pl}$  the plasma frequency, given by [36]:

$$\omega_{pl} = \frac{N_e e^2}{m_e \varepsilon_0}, \quad 6$$

where  $e$  is the elementary charge,  $m_e$  the conduction band electron mass and  $\varepsilon_0$  the vacuum permittivity.

It is important to note that the scattering time of the conduction electrons is also dependent on the carrier density, as a higher carrier density will decrease the time between scattering events. In general, the scattering time  $\tau$  (inverse of the scattering rate  $\gamma$ ) is expressed in terms of a constant electron–phonon ( $e$ – $p$ ) term and a carrier or electron-temperature dependent term ( $c$ – $c$ ) [17]:

$$\tau(N) = \frac{1}{\gamma(N)} = \frac{1}{\gamma_{e-p}} + \frac{1}{\gamma_{c-c}(N)} \quad 7$$

In case a large fraction of valence band electrons is excited, their contribution to the dielectric background of the unexcited material vanishes and as such, an alternative description for the dielectric “constant” ( $\varepsilon_b$ ) must be incorporated into the dielectric function (Eq. 5). Guizard *et al.* suggested a description derived from the Clausius–Mossotti equation [37].

While the complex dielectric function can be accessed e.g. by time-resolved ellipsometry measurements, as demonstrated e.g. by Møller *et al.* [38], our experiments, discussed below, are only able to access the real and imaginary part of the complex refractive index.

The complex dielectric function and the complex refractive index are related via [36]:

$$\sqrt{\varepsilon} = \tilde{n} = n + ik \quad 8$$

With the real part of the refractive index  $n$  and  $k$ , the imaginary part.

From equations (5) and (8), it becomes clear, that the creation of a high carrier density will lead to a decrease in the real part of the refractive index, while the imaginary part, linked to the absorption coefficient  $\alpha = 2\kappa\omega/c$ , increases.

### 2.2.2 Measuring optical properties of laser excited dielectrics – Imaging Spectral Interferometry

To measure changes of the dielectric function and the refractive index modifications of an excited dielectric material, optical pump probe spectroscopy has proven to be an excellent tool. While straightforward time-resolved transmission/absorption and reflection measurements can be used to track the overall charge carrier dynamics, information about the real part of the refractive index cannot be obtained. In addition, these techniques often lack high sensitivities for excitation densities far below the ablation threshold.

Interferometric measurement techniques, on the other hand, can provide complete information about changing optical properties, allowing the measurement of both the real part of the complex absorption index and the imaginary part at the same time.

In spatial interferometry [39], samples are placed in one arm of a Mach–Zehnder interferometer and are excited by a strong ultrashort laser pulse. The interferometric images are then produced by the interference of the probe pulse passing through the dielectric sample with a reference pulse propagating in the other arm of the interferometer. The phase and amplitude obtained by direct evaluation or via Fourier analysis of the interference picture provides the complex refractive index of the excited dielectric sample. While spatial interferometry has the ability to monitor the excitation dynamics on long timescales due to the possibility of a very long arm length

in the interferometer, the experimental set-up is complicated and sensitive to the ambient conditions of the experiment, like air turbulences, temperature fluctuations or mechanical vibrations.

Spectral interferometry [40] is, on the other hand, a technique which combines the advantages of spatial interferometry but with a much-reduced experimental effort. Here, probe and reference pulses co-propagate through a dielectric sample, only separated by a fixed time delay. The excitation by the pump pulse is placed after the reference but before the probe pulse. Typically, probe and reference pulses are created by using a Michelson interferometer-based arrangement [41, 42] but we will present a simpler and more stable common-path setup below. After interaction with the excited sample the pulses are sent to an imaging spectrometer, where a frequency-domain interference is produced. Even though the pulses are well separated in time, spatially splitting the spectrum into separate spectral components detected by the spectrometer (-pixel) leads to interference because the temporal length of an ultrashort laser pulse is defined by its bandwidth. Each pixel detects just a small partial bandwidth and therefore the individual pulses are stretched enough to interfere. The shift of the interference-fringe mini/maxima and the change of their contrast, compared to interference without excitation, give direct access to the changed real and imaginary part of the refractive index the probe pulse experiences after excitation, as we will discuss further below. One limitation of spectral interferometry is usually the temporal window available for a direct measurement of the changed optical properties. Unfortunately, a large temporal separation between reference and probe pulse requires a high-resolution spectrometer to allow the interference of both pulses within the spectrometer. While the often-used semi-common-path arrangements of a Michelson-type interferometer for spectral interferometry brings advantages compared to the Mach-Zehnder-Type, mechanical stability remains one of the downsides of both approaches.

As we want to study the effects of temporally asymmetrically shaped laser pulses, which extend to a few picoseconds as seen in Fig. 1, we utilized a measurement scheme [35, 43–45] that allows a wide measurement window of 6.5 ps and excellent spectral resolution. At the same time our approach has no need for a physical interferometry setup.

Figure 2 shows the principal set-up of our ultra-stable common-path imaging spectral interference setup, as presented, and discussed in more detail in [35, 44, 45]. We utilize 800 nm, 30 fs femtosecond laser pulses provided by a Femtolasers Femtopower Pro Amplifier System which are split into a pump and probe (and reference) arm. In the probe arm, which can be delayed with respect to the pump arm using a high-precision motorized delay stage, we frequency double the fundamental beam in a  $\beta$ -BBO crystal and pre-compress it in a prism-compressor, allowing for close to bandwidth limited pulses in the interaction area.

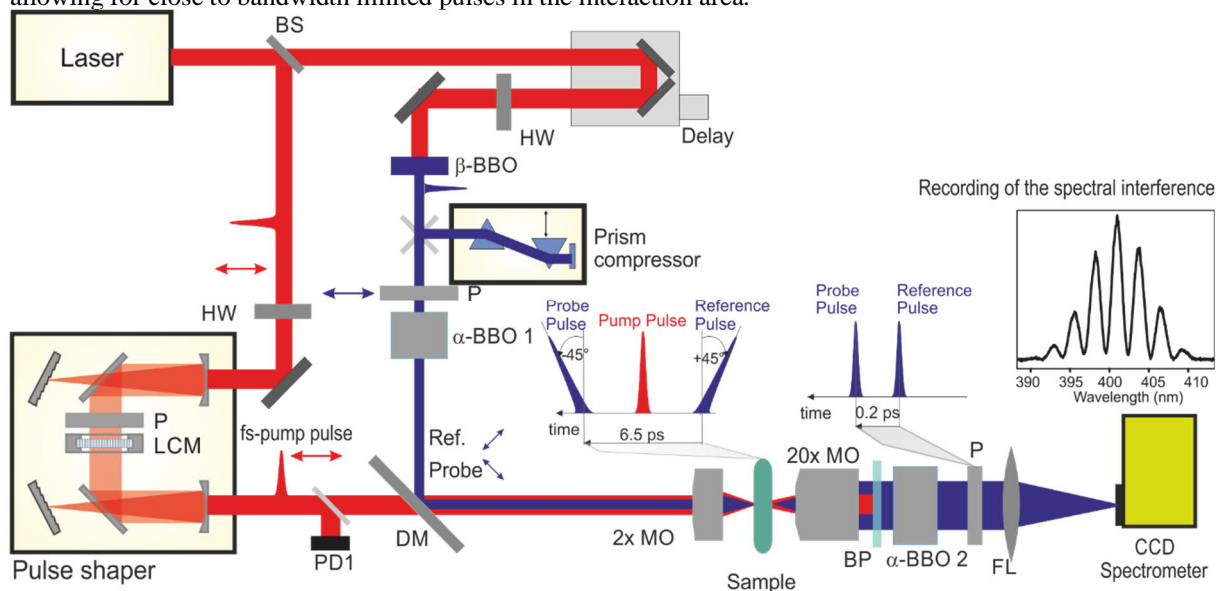


Figure 2. Experimental setup – description in the text: BS – beamsplitter. HW – half waveplate, P – polarizer, LCM – liquid crystal modulator. DM – dichroic mirror, MO – microscope objective, WJ – free flowing planar water jet, SP – short pass filter, FL – focusing lens, PBS – pellicle beamsplitter. A time-delayed pulse is frequency-doubled to 400 nm and passes through a birefringent crystal  $\alpha$ -BBO 1. This one creates a pair of orthogonally polarized pulses with a separation of 6.5 ps. The reference and probe pulses propagate through the interaction area together with the pump and probe the changes in the optical properties. A second birefringent crystal  $\alpha$ -BBO 2 decreases the temporal separation between the blue pulses to 0.2 ps. After passing through a polarizer the

*frequency-domain interference pattern is recorded – sketched above the CCD Spectrometer. Adapted from [44] with permission from Elsevier.*

Afterwards, we split the 400 nm beam into a pair of pulses in a 12.5 mm thick birefringent  $\alpha$ -BBO crystal (in Fig. 2  $\alpha$ -BBO 1). The pulses have orthogonal polarization to each other and  $\pm 45$  deg relative to the pump pulse. The resulting reference and probe pulse are separated by a temporal distance of 6.5 ps with a FWHM pulse duration of approx. 40 fs respectively. Both pulses are focused together with the temporally shaped fundamental 800 nm pump pulse of 30 fs FWHM onto the surface of a free-flowing water jet, using a long working distance apochromatic microscope objective (Mitutoyo M Plan APO 2x). The jet is produced by pumping double-deionized water through a polished stainless steel nozzle and has an average thickness of 121.3  $\mu\text{m}$  with a variation of  $\pm 0.5$   $\mu\text{m}$ , obtained by several measurements at the same position using the spectral interference signal from the internally reflected pulse. A sufficient flowrate of the water allows for a fresh volume of water each time the laser is fired (1 kHz repetition rate).

The pump arm of the setup contains a liquid crystal modulator-based home-build pulse shaper [32], which we use to apply the strong third-order dispersion to create the temporal Airy pulses, as described in section 2.1. At the same time, we make use of a thin film polarizer in the pulse shaper and a motor-controlled half-wave plate to adjust the pump pulse energy. Afterwards, pump and probe beam are recombined by a dichroic beamsplitter and focused onto the water jet.

After the pump pulse excited the water jet, it is removed from the beamline by a bandpass filter (40 nm FWHM, centered at 400 nm), inhibiting it from entering into an infinity-corrected long-working-distance apochromatic microscope objective (Mitutoyo M Plan APO 20 $\times$ ). Focused on the front-surface of the water jet, this objective collects reference and probe pulse.

As the temporal separation of 6.5 ps is too large to allow the observation of spectral-interference in our spectrometer, we utilize a second alpha-BBO crystal to reduce the temporal separation of the 400 nm pulses. By orienting the 12.2 mm thick crystal such that reference and probe are now propagating through the opposite axis compared to the first crystal, we reduce the temporal separation to only 200 fs. Using a polarizer, set to a vertical polarization, we allow for the detection of the interference pattern (see Fig.2). Afterwards, both pulses are imaged onto the entrance slit of an imaging spectrometer (Princeton Instruments 320) using a 400 mm focusing lens, providing an overall magnification of the imaging system of 40x. Thanks to the cooled 2D CCD array of the spectrometer the spectral information can be detected simultaneously along a line through the beam profile. Here, 128 pixels are available for the spatial and 1024 pixels for the spectral detection. This technique allows to record the spectral interference signal as a function of the radial position across the excitation region. A fraction of the reference-probe beam is imaged onto a CCD camera, which allows for a high precision in overlapping pump and probe beam on the surface of the water jet. It is important to notice that the beam sizes of pump and probe pulse were chosen such that the Rayleigh range of both pulses exceeded the water jet's thickness by more than one order of magnitude, ensuring a homogeneous illumination of the jet.

In the previous section, we described the impact of the excitation of electrons into the conduction band on the complex dielectric function and consequentially the real and imaginary part of the refractive index. Using our time-resolved spectral interferometry setup we probe the difference of the refractive indices between excited and un-excited state [35, 44]:

$$\Delta\tilde{n}(N) = \tilde{n}(N) - \tilde{n}(N = 0) = -\frac{1}{2n_0} \left(\frac{\omega_{pl}}{\omega}\right)^2 \frac{1}{1 - (i\omega\tau)^{-1}} \quad 9$$

with  $n_0 = \sqrt{\epsilon_B}$ .

It is important to note, that the probe pulse measures the accumulated refractive index change throughout the water jet, thus being unable to provide a spatial resolution in depth. Consequentially could different distributions of refractive index change lead to the same overall refractive index change, as discussed in detail below.

The two main observations from the interference pattern mentioned above, fringe-shift and -contrast, relate to the real and complex part as follows:

**The phase shift:**

The lowered real part of the complex refractive index (due to the excitation of carriers) leads to a higher phase velocity of the probe pulse in the water jet which results in a decreased temporal separation between the probe and reference pulse. This reduced temporal separation is measured as a phase shift  $\Delta\Phi$  in the spectral interference pattern (i.e. a shift of the position of the interference minima/maxima) and is highly dependent on the carrier density and the thickness of the sample  $L$  [35, 44]:

$$\Delta\Phi(N) = \frac{2\pi}{\lambda} \int_{z=0}^L \text{Re}(\Delta\tilde{n}(N)) dz \quad 10$$

### The optical density:

The increased absorption by free carriers leads to the absorption of the probe pulse (a reduction in interference contrast) and is typically given as the optical density via the relation [35, 44]:

$$\text{OD} = -\ln T = \frac{4\pi}{\lambda} \int_{z=0}^L \text{Im}(\Delta\tilde{n}(N)) dz \quad 11$$

where  $T$  is the transmission.

While the reflectivity at the surface of the water jet is also impacted by the change in the refractive index, at excitation densities well below the ablation threshold, its impact onto the measured optical density/absorption can be neglected and absorption inside the sample dominates the change in transmission.

Although both values, phase shift and optical density, can be extracted right away from the interference pattern, as mentioned above, the Fourier-transform analysis provides a significant improvement allowing for a much more sensitive and reliable evaluation of the abovementioned properties. A detailed description of the data evaluation can be found in [35, 44, 45].

### 2.2.3. Spatially resolved measurement of laser excitation in water with ultrashort and temporal Airy pulses

To demonstrate the peculiarities of laser excitation with temporal Airy pulses, we compare the excitation created by a 30 fs 800 nm bandwidth-limited laser pulse and a positive temporal Airy pulse. From the temporal profile of both pulse shapes (a symmetrical Gaussian beam with a FWHM of 30 fs and the positive TAP pulse shown in Fig. 1) it becomes apparent that the temporal evolution of the electron density created by each of the pulses is very different. Unfortunately, it is not possible to fully resolve the initial temporal change of the refractive index (increase absorption and decrease of the phase shift) of both pulse shapes precisely, as the measured signal is overlapped by the optical Kerr effect [35, 45]: This pump-pulse intensity dependent increase in the real part of the refractive index will hide the actual phase shift and optical density evolutions until the pump pulse has passed. Thus, we will discuss the results obtained shortly after the pump pulse has passed the sample. This allows to measure the optical properties before significant carrier recombination and diffusion, which is typically set on a 10s to 100s of picosecond timescale [45]. The results discussed below were obtained in a close collaboration with the research group of Peter Balling at Aarhus University.

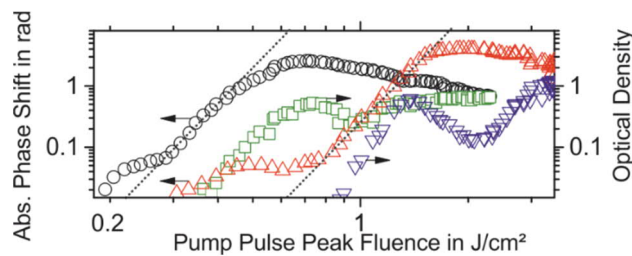


Figure 3 - Measured pump-pulse fluence dependent excitation of liquid water: Black circles - absolute phase shift for BWL pulses; Red up pointed triangles - absolute phase shift for TAP pulses; Green squares - Optical density for BWL pulses; Purple down pointing triangles - Optical density for TAP pulses. The black dotted lines indicate power law scaling of 6. Please note that the measured phase shift is negative. Reproduced from [44] with permission from Elsevier.

As a first step in understanding the excitation of water, we will concentrate on the pump-pulse fluence dependence thus the dependence on the number of conduction band electrons within the sample. Figure 3 shows the locally measured phase shift and the optical density as a function of the pump pulse peak fluence for both pulse shapes. The first observation made is that the detection of a change in the phase shift (black circles, red triangles) happens at a significantly lower excitation fluence compared to the measured optical density (green squares, blue down pointing triangles). This is due to the much higher sensitivity of the measurement to the real part of the dielectric function compared to the imaginary part (absorption).

In addition, we make two major observations:

**1. The threshold for excitation and the subsequent change of phase shift and optical density is significantly higher for the TAP pulse compared to the BWL.**

The black dotted lines in Fig. 3 indicate a power-law scaling with the order of 6, perfectly fitting a multi-photon process involving six 800 nm photons, with a photon energy of 1.55eV, to promote electrons across the estimated bandgap energy of around 8.3 eV to 9.5 eV [46, 47]. The reason for the difference in the excitation thresholds can be found in the significantly different peak intensity of the two pulse shapes. The peak of the main pulse of the TAP pulse train has roughly only 1/6<sup>th</sup> of the intensity compared to the BWL pulse. Consequentially, the required fluence to initiate multi-photon excitation (as the seed for avalanche processes) is higher for the TAP pulse. This has been discussed in more detail in our previous work [35].

In addition, we observe a small increase in phase shift starting at very low excitation fluences and stagnating until the main excitation takes place (indicated by the black dotted line, which follows a power law scaling of 6). This low stagnating signal is indicative for a lower order excitation process from a low-density reservoir, such as solvated electrons [47, 48], which have caught large attention throughout recent years, and which added to the intense discussions about the bandgap energy of water [46–48]. However, it also becomes apparent that the density of carriers injected via this pathway are too low to initiate a subsequent excitation process via the avalanche process, hence the stagnation of the signal for increasing carrier density. We estimate the carrier density of the low-density reservoir to be  $1.4 \times 10^{18} \text{ cm}^{-3}$  under the assumption of a constant electron density throughout the water jet (Eq. 10).

**2. We observe that the maximum change in the phase shift and optical density is significantly higher for the TAP compared to the BWL pulse.**

To understand how the TAP pulse can – irrespectively of the peak fluence/excitation strength – create a much higher phase shift and optical density throughout the water jet, we will make use of our simplified rate equation model described in section 2.1. To model the experimental observations, we calculate the excitation throughout the material, taking into account the absorption of the exciting pulse by multiphoton and free carrier absorption [44]. Afterwards we calculate the accumulated phase shift and optical density by the probe pulse according to equations (10) and (11).

Figure 4 shows the calculated carrier density distribution in the water jet for both the BWL and the TAP pulse as a function of the radial position at the surface (a), and as a function of depth at the center of the beam (b). While the depth-dependent distribution (b) caused by the BWL pulse (black curve) shows that with increasing depth the carrier density drastically decreases, the TAP pulse (red dashed curve) shows a quite different distribution. Although the general behavior remains the same, for an equal strong carrier density at the surface, the electron density is much higher throughout the material causing a larger accumulated local phase shift.

The reason for this behavior can be found in the unique temporal profile of the TAP pulse, already discussed in section 2. As the carrier density only slowly increases with time and is delayed due to peculiarities of the avalanche excitation process, the highest carrier density will overlap with the least intense parts of the pulse, allowing it to propagate deep into the material. The BWL on the other hand causes a rapid excitation of the large fraction of carriers directly at the surface of the water jet leading to a strong absorption of the pump pulse preventing it to propagate deep into the material. While a simply chirped pulse would certainly lead to similar results, it is important to notice that the pulse energy required would be significantly higher, as the first, low-intensity half of the pulse duration usually does not lead to an excitation (similar to the negative TAP, see Fig. 1) and only the peak part and subsequent rest of the pulse are absorbed. This aspect is further discussed in section 3.

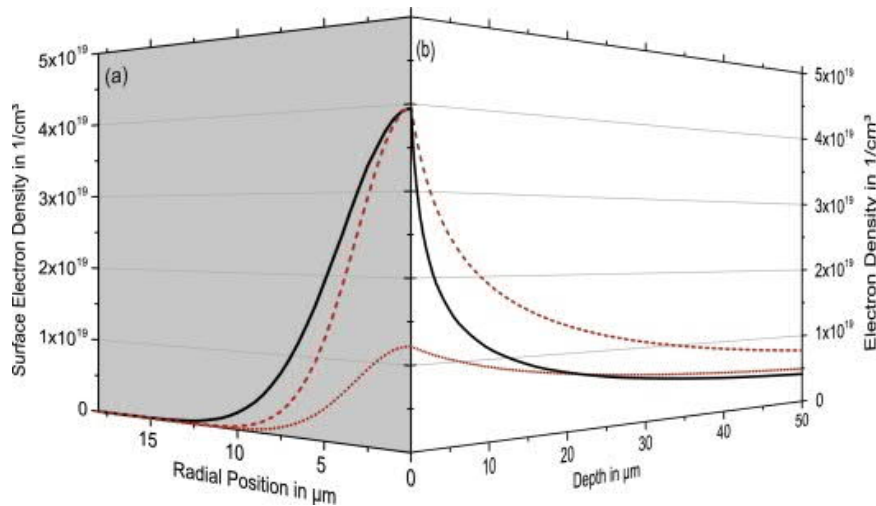


Figure 3 Simulated radially- and depth-dependent phase shift for BWL (black) and TAP (red) laser pulses: (a) radially dependent phase shift for: equal phase shift at  $r=0 \mu\text{m}$  (red dotted line). Equal electron density at  $r=0 \mu\text{m}$  (red dashed line). (b) Depth-dependent conduction band electron density at the center of the laser pulse ( $r=0 \mu\text{m}$ ) for the same cases as in (a). Detailed information about the simulations are given in [44]. Reproduced from [44] with permission from Elsevier.

The dependence of the excitation on the local pump pulse fluence, discussed above, also heavily influence the radial distribution of the carrier density, as typically Gaussian beam profiles are used for laser excitation and material processing. Figure 4 (a) shows the calculated radial dependence on the carrier density at the surface of the water jet using BWL (black line) and TAP (red dashed line) pulses. While with increasing radial position (and thus lower local fluence) the surface carrier density strongly decreases for both pulse shapes (starting at the same value in the center), it decreases more quickly for the TAP pulse compared to the BWL pulse, strongly reducing the excited area by approx. a factor of 2.

[44]

To confirm that our simulations capture the influence of the temporal pulse shape on the spatial carrier distribution throughout the water jet, we compare it to the phase shift measured along the radius of the pump pulse using our imaging setup described above.

Figure 5 (b) shows the radial distribution of the measured phase shift using the BWL (black circles) and TAP pulse (red triangles) and the corresponding simulations (black solid and red dashed lines) for the case of an equally strong carrier density at the surface in the center of the laser pulse. We observe an excellent agreement between simulation and experiment which proves the significantly larger phase shift in the center by the larger integrated carrier density of the TAP pulse. In addition, a narrower phase shift distribution for the latter is observed.

Furthermore, it is interesting to discuss the results where an equal phase shift by both pulses is obtained, as this can wrongly be identified as the case in which the material is brought into the same excitation conditions. Here we had to choose an excitation fluence of the TAP pulse 2.2x higher compared to the BWL. The results are shown in Fig. 5 (a) and again, very good agreement between measurement and simulation for both pulse shapes are obtained, confirming that the simple model captures the interplay between multiphoton and avalanche excitation. From Fig. 4 (b) (red dotted line) we observe that the carrier densities at the surface leading to an equal measured phase shift in the center are four times lower than the density created by the BWL pulse. However, it can also be seen that the phase shift deep inside the water jet are actually higher for the TAP pulse compared to the BWL.

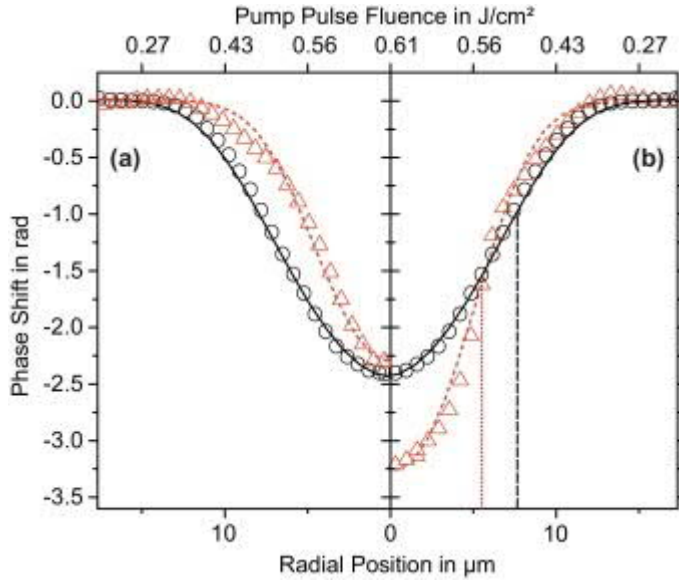


Figure 4 Measured (symbols) and simulated (lines) radially dependent phase shift for BWL (black) and TAP (red) laser pulses: (a) equal measured phase shift at  $r=0 \mu\text{m}$  for both pulse shapes. For the TAP the fluence is increased by a factor of 2.2. (b) Equal simulated electron density at the surface at  $r=0 \mu\text{m}$  for both pulse shapes. The fluence for TAP is increased by a factor of 2.5. Black dashed and red dotted vertical lines indicate the radius at which the phase shift decreased to half of the minimum value. The simulation details can be found here [44]. Reproduced with permission from [44] with permission from Elsevier.

Overall, our spatially-resolved measurements on water demonstrate that temporal Airy pulses advantageously make use of the heat and seed model, allowing the pulse to create a high carrier density deep into the material over a smaller area, causing a “needle-like” excitation profile in strong contrast to the excitation by the BWL that has a larger lateral but much smaller longitudinal extension thereby allowing material processing only close to the surface and with less spatial resolution than the TAP.

### 3 Proof of principle: Nanostructuring of solid dielectrics at the nanoscale with temporal Airy pulses

We have discussed the initial step in the processing of dielectric materials, the carrier excitation and the impact of temporal pulse shaping on its spatial properties. Here, we will demonstrate the long-lasting impact of the initial carrier distribution by discussing material processing experiments in which positive TAP pulses are able to create deeper and thinner ablation structures in sapphire and fused silica.

The results presented in the upcoming sections 3.1 and 3.2 were obtained in a close collaboration with the research groups of Javier Solis and Jan Siegel at the Spanish National Research Council, as well as with the group of Hartmuth Hillmer at the University of Kassel, respectively.

#### 3.1 Post-mortem measurements of laser ablation in sapphire

To link the carrier excitation distribution discussed in the last section to permanent material modifications we performed single shot laser processing experiments on crystalline sapphire [49]. Sapphire, a crystalline solid dielectric with a high bandgap (approx. 10 eV), shares the main excitation pathways with water and thus provides the perfect platform to demonstrate the possibilities of the TAP pulses and to link the initial carrier distribution to the final ablation profile. Using the same pulse shaping approach as in our water experiments, BWL and TAP pulses are tightly focused onto the surface of a sapphire sample and the resulting hole structures are investigated post-mortem via atomic force microscopy.

Figure 6 shows AFM images and profiles of hole structures obtained by a single BWL (at 89 nJ) and TAP (at 97 nJ). It can be seen that for the TAP pulse a smaller hole diameter with a larger depth compared to the BWL pulse is obtained, thus representing a similar profile to what has been obtained in the spectral interference measurements. Even if the pulse energy would be tuned for the BWL to create a smaller diameter to match the TAP hole surface diameter, the depth would reduce significantly as well, giving the TAP a unique ablation profile. These measurements demonstrate and confirm that the electronic excitation mechanisms observed in the real time measurements in water are at play in the permanent material modification of solid dielectrics. Note that both processes occur on time scales differing by many orders of magnitude.

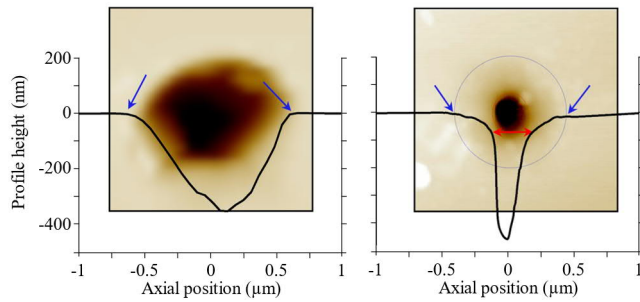


Figure 5 AFM micrographs overlaid with depth cross sections (black line) of two craters produced using a BWL pulse at 89 nJ (left) and a positive TAP pulse at 97 nJ (right), both with a beam diameter of 1.4  $\mu\text{m}$ . The arrows and dotted lines indicate the border of the different ablation regimes, evidenced as a slope change in the depth cross sections. Adapted from [49], Copyright 2015 American Chemical Society.

### 3.2 High-aspect ratio ablation structures in fused silica

Another material well-suited for processing with temporal airy pulses is fused silica. In contrast to water or sapphire, conduction band electrons are – shortly after excitation – quickly captured into self-trapped exciton states on a typical timescale of 100–200 fs [41, 45]. The self-trapped excitons, which are energetically localized in the middle of the bandgap, typically only contribute with a positive refractive index modification to the optical properties and do not absorb single photons in the visible or near UV spectral range [50]. While the trapping of electrons has no or only little impact on the excitation profile and energy deposition into the material by ultrashort BWL laser pulses, the dynamics are heavily changed for the temporal Airy pulses as electrons are being trapped continuously during the interaction with the pulses. This is especially important, as trapped electrons can be excited back into the conduction band via multiphoton and avalanche excitation [33, 50].

As the required energy and thus photonicity for promoting electrons from the trapping states to the conduction band is smaller (only 5.4 eV) compared to the main excitation channel from the valence to the conduction band (9 eV), the TAP pulse can efficiently deposit energy deep into the material [33]. This is because the cross section for a multi-photon process heavily decreases with the order of photons required to drive the process. At the same time excitonic trapping will keep the overall conduction band carrier density low, leading to only a small amount of free carrier absorption [33]. The complex interaction between excitation, trapping and re-excitation strongly enhances the spatial features brought by the TAP pulse (and thus its energy deposition into the material) which is demonstrated in Fig. 7.

The difference in the ablation characteristics of BWL and TAP pulses under different focus positions (below, at or above the surface) are shown in Fig. 7 (b) through (d). These side-views of the ablation structures were obtained by focused ion beam milling and scanning electron microscopy.

Figure 7 (b) exemplifies that BWL pulses only create a shallow ablation structure, reaching only a couple of hundreds of nm into the fused silica (independent on the focus position). Even if the pulse energy is increased by a factor of 2.5 (Fig. 7 (c)), thus 5x higher than the ablation threshold, the depth of the ablation structure does not increase, while the lateral ablation radius grows. This behavior is not only linked to a strong absorption and self-reflection of the BWL pulse due to the excitation of the fused silica close to the surface, but also by a strong absorption in the air above the sample. Our simulations of the ablation region (shaded area) – shown to the right of the SEM images – which take the latter effect into account and are able to capture the stagnation of the hole depth by the BWL laser pulse [33].

In Fig. 7 (d), hole structures obtained with a single TAP pulse, with a pulse energy 2.5x above the ablation threshold, for the three focus positions are shown. It becomes immediately clear, that the TAP pulse is able to create a needle-shaped high aspect-ratio ablation structure reaching ratios up to 30:1 (depth to channel width). While the simulations are not able to fully predict the ablation diameter – possibly due to not all of the material being ejected, as well as refraction and propagation effects not being considered – the depth predictions fit exceptionally well (see [33] and the corresponding supplementary material for additional data and in-depth discussions). This demonstrates that due to the continuous trapping of carriers, the TAP pulse is able to penetrate deep into the material depositing a huge amount of energy by having a low peak intensity, making it the perfect tool for high aspect ratio material processing, avoiding large absorption above and inside the material. An important observation made from our experiments and simulations is that the ablation depth achieved by the TAP

pulse is directly linked to its Rayleigh range, thus purely defined by the spot size and wavelength, and not related to any filamentation phenomena [51, 52].

In section 2 we discussed that laser pulses with long pulse durations should – in principle – be able to produce the same excitation volume compared to TAP+, just at the price of a higher pulse energy, as nearly half of the pulse is wasted before the intensity is high enough to reach the threshold for strong-field excitation. In the case of the processing of fused silica, however, the simply longer pulses have more than just the energetic disadvantage. Figure 7 (e) shows the ablation structures obtained with a symmetrically stretched – by applying a linear chirp – pulse with the same statistical pulse duration (i.e. the time in which light is present) as the TAP+ pulse. While we observe that the stretched pulse is also able to create deep ablation channels, it is obvious that the channel width is larger (reducing the aspect ratio) and the hole structure is not as “clean” as the ones created by the TAP pulses. The reason for this reduced processing quality and precision can be related to two main aspects: 1. The continuous presence of the light field will lead to conduction band electrons gaining much higher kinetic energies, leading to a larger diffusion volume of the carriers and consequentially an energy that is deposited over a larger radius, while the TAP+ pulse causes a much more localized energy input, as electrons are trapped close to their excitation location. 2. Femtosecond laser amplifier systems often suffer from a slight spatial chirp (i.e. the distribution of frequencies across the spatial beam profile). Thus, when temporally stretched (chirped) pulses are used, there is a slight temporal delay between different spatial parts of the beam, exciting and ablating the material inhomogeneously as e.g. higher photon energies lead to a slightly lower ablation threshold compared to parts of the beam where first low energy photons arrive, adding to the asymmetric shape of the ablation structure [53].

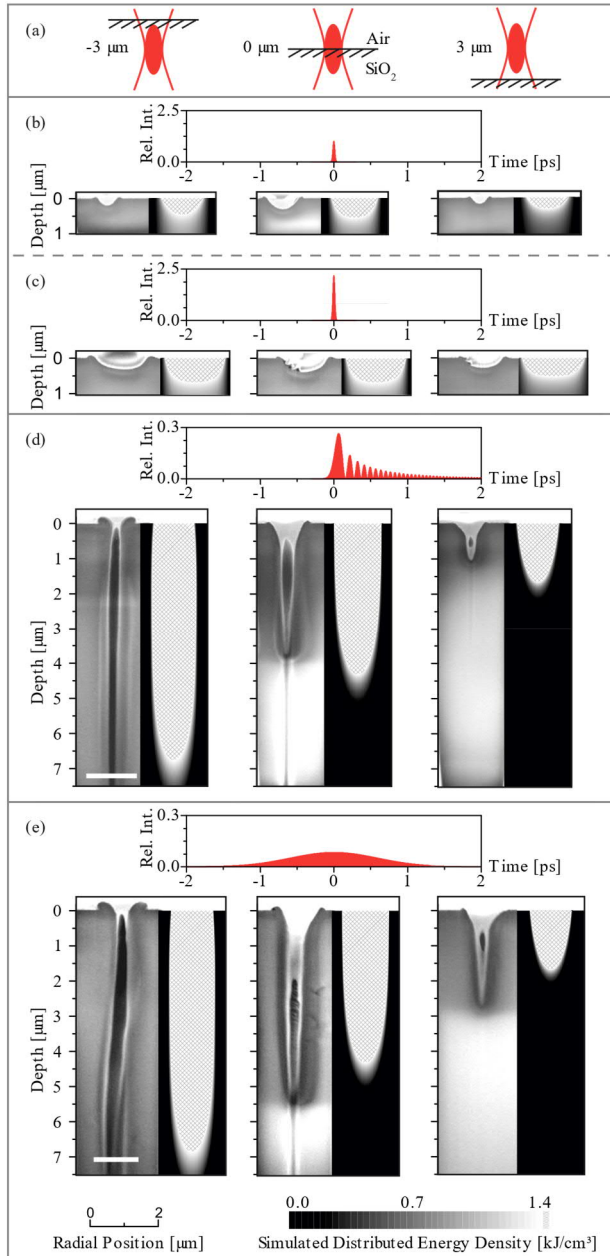


Figure 6, Machining results for (b), (c) bandwidth-limited pulses, (d) TAPs with a third order dispersion coefficient of  $6 \times 10^5 \text{ fs}^3$ , and (e) temporally symmetric chirped pulses with a second order dispersion coefficient of  $1.5 \times 10^4 \text{ fs}^2$  at three different focus positions with respect to the surface of the fused silica sample as indicated in (a). For each focus position, scanning electron microscope images of cross-sections obtained by focused ion beam (FIB) milling (left) are compared to simulations (right). The shaded areas in the simulation areas indicate where an – for the ablation required – energy of at least  $1.4 \text{ kJ/cm}^3$  was deposited by the laser pulse. Experiments in (b), (d), and (e) were performed at approximately  $2.5 \times$  above the ablation threshold energy for the corresponding pulse shape. Results for bandwidth-limited pulses approximately 6 times above their threshold and corresponding to the same pulse energy as used for shaped pulses in (d) are displayed in (c) showing shallow structures. The peak intensities of the applied pulses in the pulse pictograms are normalized to the simulated BWL shown in (b). The dark shaded areas around the holes in the scanning electron microscope images are attributed to densified material after material processing. Vertical white lines in the middle column in (d) and (e) are FIB milling artifacts, and horizontal white bars in (d) and (e) indicate the measured hole depth. Reproduced from [33] with permission from the Optical Society America.

#### 4 Optoporation of biological cells with temporal Airy pulses

After having demonstrated the control of direct nanostructuring of solid dielectrics, we will now take a look at nanostructuring of biological cells in an aqueous environment, where the damage to the cell's membrane is mediated by the excitation of water and consequent generation of cavitation bubbles. Here, the control over the shape of the excited region by temporal pulse shaping, discussed in section 2, offers significant advantages regarding targeting the cell membrane. The results discussed below were obtained in close collaboration with the group of Jean Pierre Wolf at University of Geneva, Switzerland [54, 55].

Introducing foreign molecules into living cells is an important part of the toolbox of biologists. While the cell membrane is permeable for some molecules, non-permeable molecules must be delivered by artificial means (transfection) like transient chemical bond breaking or physical disruption of the membrane. Next to established large scale technologies like electrophoreses or viral vectors, ultrashort laser pulses can be used to create a transient pore in the cell membrane through which molecules can enter the cell. In a microscope setup it is possible to target single cells.

For an extensive review of different poration techniques and their application in different areas of research see for example [56] or [57]. The pathway from laser excitation of water to the generation of cavitation bubbles and how they can disturb the cell membrane is laid out in [30] and in chapter 38.

Depending on the pulse parameters (energy, number of pulses, wavelength, pulse length) two regimes of laser-cell membrane interaction for optoporation can be differentiated: chemically induced damage with a large number of low intensity pulses, where the energy absorbed by the water can, for example, create free radicals that destruct the cell membrane; Or, damage by cavitation bubbles, where the high local excitation of the water by a high intensity pulse is so strong that short lived bubbles form and cause physical stress to the membrane [30]. In the following we will discuss poration with a single femtosecond laser pulse with energies above the reported intensity threshold for bubble formation in water with ultrashort 800 nm femtosecond laser pulses ( $10^{14}\text{W}/\text{cm}^2$ ).

When focusing the laser with a high numerical aperture microscope objective onto the cell, the affected region is micrometer-sized while the irregularly shaped cells can be several tens of micrometer in size. As a test system we use the well known HeLa cervical cancer cells (HeLa meaning Henrietta Lacks, the person from whom the line of cells was started in 1951) [58–60]. These cells exhibit a fried egg shape where the majority of the cell is relatively flat with a height of 5–7  $\mu\text{m}$  and the nucleus forming a highpoint bulging upwards as sketched in Fig. 8. To target a cell's membrane with a laser beam on these scales, precise positioning in all three spatial dimensions is necessary. This can be challenging and time-consuming. As discussed above, the width and length of the excited region can be controlled by tuning the temporal shape of the laser pulse, especially featuring the needle-shaped interaction region achieved with TAP pulses. This high spatial aspect ratio reduces the need for exact targeting in vertical direction while keeping the affected volume small.

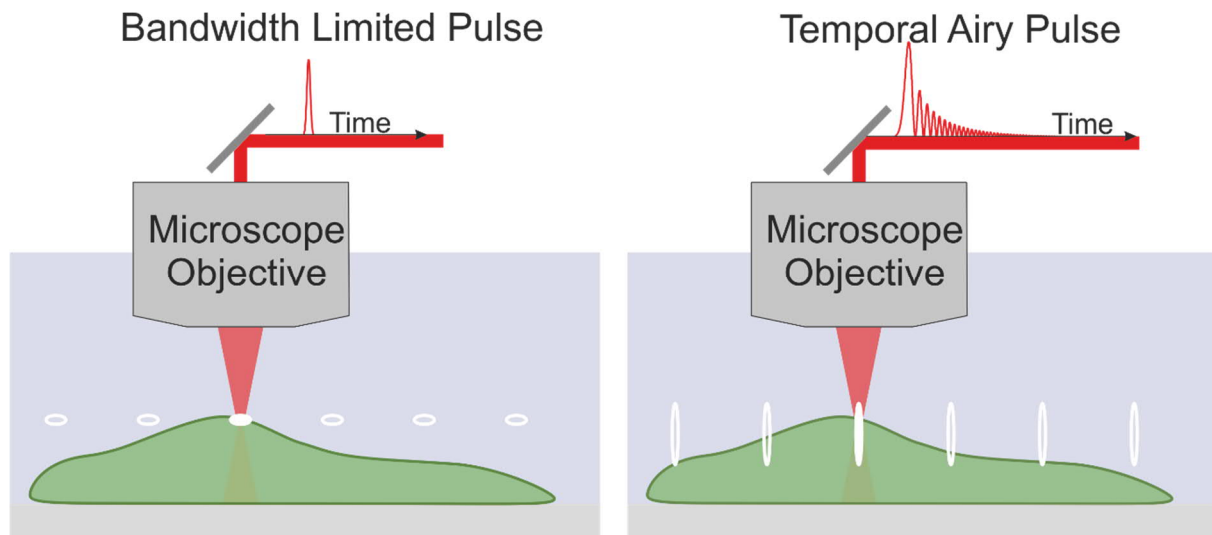


*Figure 8. Sketch of irregularly shaped HeLa cell (green) and focused 800 nm laser beams (red) using bandwidth limited pulses (left) and positive TAP (right). The use of TAPs assures high-aspect ratio needle-like excitation regions in the surrounding water for every laser shot as sketched in white and therefore provides a higher chance to porate the membrane of the cell in comparison to the highly localized excitation by the BWL pulse (left).*

We have investigated the effect of temporal pulse shaping on the laser-cell membrane interaction of HeLa cells in water. In a first study, fixed cells were processed, and the resulting damage was analyzed with SEM [54]. In a second step, the same nanostructuring was applied to living cells and the poration efficiency and survivability were evaluated with fluorescent dyes [55].

In both studies, a monolayer of HeLa cells was grown on a substrate and processed with single laser pulses by raster-scanning at a fixed vertical position. The 30 fs, 800 nm pulses were focused with a 40x, 0.75 NA water immersion objective to a focal spot with an assumed beam waist of 0.7  $\mu\text{m}$ . The vertical position of the focus was set at 6  $\mu\text{m}$  above the substrate surface and corresponds to the mean thickness of the layer of cells. The matrix pattern of laser shot position had a shot-to-shot distance of 7.5  $\mu\text{m}$ . For the SEM analysis of the fixed cells, reference marks and labeling were placed into the glass cover slip in a 100  $\mu\text{m}$  distance around the matrix to locate the matrix positions in the later analysis. It is interesting to note that much higher pulse energies are needed for processing of the glass substrate than for processing the cell membrane (1  $\mu\text{J}$  compared to around 100 nJ for cells). When using BWL pulses, the localized excitation in the water medium is so high that big cavitation bubbles and shockwaves lead to the detachment of several cells in a significant radius. This was prevented by using TAP+

pulses with a third order dispersion coefficient of only 100 kfs<sup>3</sup> and focusing directly onto the surface of the glass substrate.

For the processing of fixed and living cells, BWL (bandwidth limited pulses), TAP+ (temporal Airy pulse with a third order dispersion of +600000 fs<sup>3</sup>), TAP- (temporal Airy pulses with a third order dispersion of -600000 fs<sup>3</sup>) and GDD (linearly positively chirped pulses with a group delay dispersion of +15000 fs<sup>2</sup>) were used.

#### 4.1 Optoporation of fixed cells: Efficiency and morphology

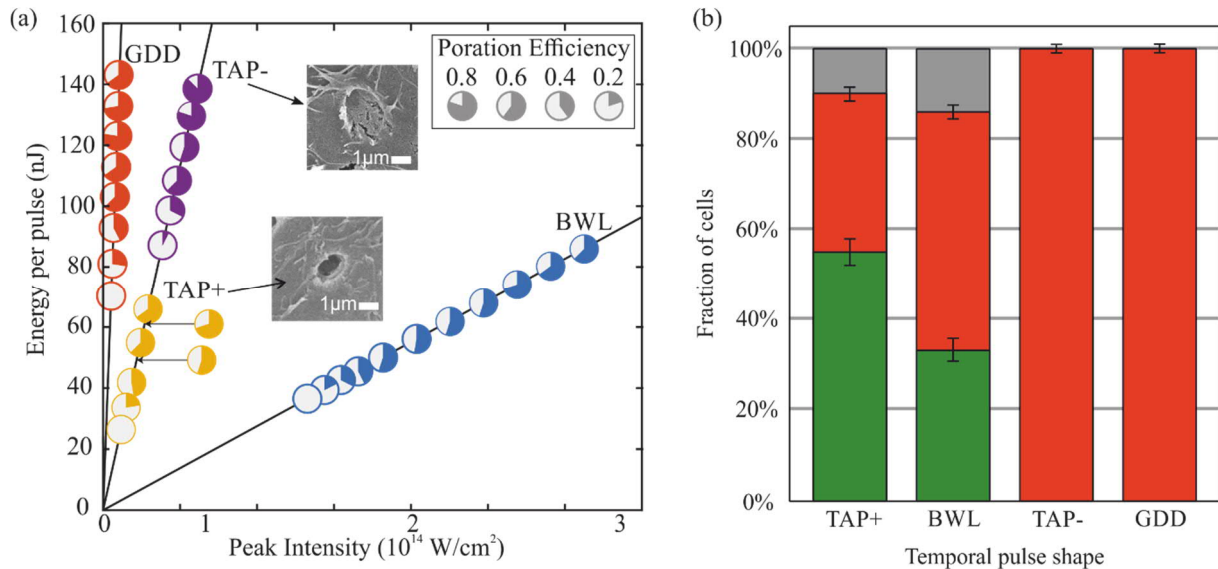


Figure 9: (a), Poration efficiency of fixed HeLa cells irradiated with BWL (bandwidth limited), TAP+ (temporal Airy pulse with a third order dispersion of +600000 fs<sup>3</sup>), TAP- (temporal Airy pulses with a third order dispersion of -600000 fs<sup>3</sup>) and GDD (linearly positively chirped pulses with a group delay dispersion of +15000 fs<sup>2</sup>). For each pulse shape and single pulse energy, a Harvey ball represent the experimentally found poration efficiency. The black lines show the energy-dependent peak intensity of a pulse depending on its shape. (b), Fraction of successfully porated cells during laser treatment (green bar) and cells alive after four hours (green plus red bar). Grey represents detached cells. All four temporal pulse shapes BWL (bandwidth limited), TAP+ (temporal Airy pulse with a third order dispersion of +600000 fs<sup>3</sup>), TAP- (temporal Airy pulses with a third order dispersion of -600000 fs<sup>3</sup>) and GDD (linearly positively chirped pulses with a group delay dispersion of +15000 fs<sup>2</sup>) were applied with the same energy of 75 nJ per pulse. Adapted from (a) [54] and (b) [55]. Copyright 2015 and 2018 American Chemical Society

In Fig. 9 (a) we present the results of the first study on fixed HeLa cells analyzed with SEM [54]. Each Harvey ball represents the ratio of successful poration for up to 32 laser spots with identical parameters (shot locations that hit a gap in the monolayer of HeLa cells were excluded from the analysis).

For the onset of poration, TAP- needs the highest pulse energy (90 nJ). For GDD around 80 nJ are needed and 40 nJ for BWL. With just 30 nJ TAP+ require the least energy. For all pulse shapes, increasing the pulse energy to twice the respective threshold enhances the poration efficiency to roughly 75 %. Taking into account the temporal shape of the pulses, all shaped pulses show significantly lower peak intensities compared to the BWL pulse. For poration efficiency around 60 %, the peak intensity of TAP+ is one order magnitude below that one of BWL.

The analysis by SEM enables us to categorize the type of damage caused by the single laser pulses. The differentiation is done between ablation type damage (round holes), recess damage (disturbed membrane structure) and larger cracks. One shot location can exhibit more than one type of damage at the same time, for example a visible hole with cracks forming at the edges. For the cracks it must be noted that they might have formed or been enhanced during the preparation of the samples for the SEM. The most notable observation is that TAP+ pulses mainly produce ablation type damage and TAP- irregular recess type damage (see inset images in Fig. 9 (a)). This points to two different situations during excitation and consequent cavitation bubble mediated disruption of the cell membrane. The TAP+ causes precise, strong but spatially confined damage which is big enough for large molecules or even nanoparticles to enter the cell.

## 4.2 Optoporation of living cells: Survivability

From the SEM imaging we can get information about the surface of the cell. But the needle-like excited region of shaped pulses makes it more likely that the excited region and consequent cavitation bubble induced damage reach into the cell. To study the possible toxicity of the poration with shaped laser pulses we performed the same nanostructuring on living HeLa cells [55]. The combination of three different fluorescent markers enabled us to identify the poration efficiency and survivability four hours after the laser treatment, by applying them before, during and after the laser, respectively. All three dyes have different wavelengths, are imaged simultaneously in a nonlinear fluorescence microscope and hundreds of cells analyzed by automated segmentation.

As Fig. 9 (b) shows, at a mid-range pulse energy of 75 nJ, the BWL and TAP+ display poration efficiencies of 33 % and 55 %, respectively. Nearly all cells survived the laser treatment in the investigated time window of four hours, independent of the poration success. For TAP- and GDD the chosen pulse energy was too low to achieve poration.

Choosing TAP+ for single cell single pulse opto-poration can provide high poration efficiency and viability of the cells by controlling the shape of the region in which nanostructuring of the cell membrane takes place. In cases where a layer of cells is scanned, or single cells (or parts of cells) are targeted, the needle-shaped effected zone lifts constraints on vertical targeting and could significantly speed up these procedures.

## 5 Summary and further application opportunities

In this chapter we have demonstrated that the utilization of temporal Airy pulses (TAP) is an enabling technique for the controlled processing of transparent matter with its unique high-aspect ratio needle-like excitation shape, ranging from applications in permanent laser ablation to the optoporation of biological tissue. We, however, imagine that the spatial control of carrier excitation by temporal pulse shaping to be of beneficial use in further applications as exemplified below.

A direct application of the elongated excitation region could be the enhancement of optical gain from multi-photon stimulated emission processes in excited dielectric materials, such as sapphire [45] and fused silica [61]: Here, the conduction band carrier density or density of self-trapped excitons acts as an energetically and spatially localized gain medium for an intense near-UV probe pulse. We have already demonstrated that control of spatial excitation distribution by temporal Airy pulses can be used to increase the gain length and consequentially increase the obtainable amplification by a factor of 3 compared to the excitation with bandwidth limited femtosecond laser pulses.

The utilization of the needle-like excitation shape offered by TAP pulses in sapphire and fused silica could offer an additional degree of freedom either in the writing of optical waveguides or the creation of microfluidic structures. In addition, we do see further applications in terms of biomedical and genetic research, where the tunable excitation depth/aspect ratio as well as the reduced peak intensities could be beneficial for an improved processing efficiency while reducing collateral damage. Also two and three photon fluorescence microscopy

## References

1. K. Sugioka, Y. Cheng, *Light Sci Appl* (2014) doi:10.1038/lssa.2014.30
2. M. Malinauskas, A. Žukauskas, S. Hasegawa, Y. Hayasaki, V. Mizeikis, R. Buividas, S. Juodkakis, *Light, science & applications* (2016) doi:10.1038/lssa.2016.133
3. S. Lei, X. Zhao, X. Yu, A. Hu, S. Vukelic, M.B.G. Jun, H.-E. Joe, Y.L. Yao, Y.C. Shin, *Journal of Manufacturing Science and Engineering* (2020) doi:10.1115/1.4045969
4. I.H. Chowdhury, X. Xu, A.M. Weiner, in *Commercial and Biomedical Applications of Ultrafast Lasers III. High-Power Lasers and Applications*, San Jose, CA, Saturday 25 January 2003 (SPIE2003), p. 138
5. I.H. Chowdhury, X. Xu, A.M. Weiner, *Appl. Phys. Lett.* (2005) doi:10.1063/1.1901806
6. Y. Qi, H. Qi, Q. Wang, Z. Chen, Z. Hu, *Optics & Laser Technology* (2015) doi:10.1016/j.optlastec.2014.06.017
7. E. Terasawa, T. Shibuya, D. Satoh, Y. Moriai, H. Ogawa, M. Tanaka, R. Kuroda, Y. Kobayashi, K. Sakaue, M. Washio, *Appl. Phys. A* (2020) doi:10.1007/s00339-020-03640-0
8. D. Giguère, G. Olivié, F. Vidal, S. Toetsch, G. Girard, T. Ozaki, J.-C. Kieffer, O. Nada, I. Brunette, *Journal of the Optical Society of America. A, Optics, image science, and vision* (2007) doi:10.1364/josaa.24.001562

9. R. Stoian, J.-P. Colombier, *Nanophotonics* (2020) doi:10.1515/nanoph-2020-0310
10. K. Sugioka, M. Meunier, A. Piqué (eds.), *Laser Precision Microfabrication* (Springer Berlin Heidelberg, Berlin, Heidelberg, 2010)
11. K. Sugioka, *Nanophotonics* (2017) doi:10.1515/nanoph-2016-0004
12. in *Optically Induced Nanostructures*, ed. by K. König, A. Ostendorf (De Gruyter 2015), p. 47
13. F. Zimmermann, S. Richter, S. Döring, A. Tünnermann, S. Nolte, *Applied optics* (2013) doi:10.1364/AO.52.001149
14. M. Domke, V. Matylytsky, S. Stroj, *Applied Surface Science* (2020) doi:10.1016/j.apsusc.2019.144594
15. C. Javaux Léger, K. Mishchik, O. Dematteo-Caulier, S. Skupin, B. Chimier, G. Duchateau, A. Bourgeade, C. Hönninger, E. Mottay, J. Lopez, R. Kling, in *Laser-based Micro- and Nanoprocessing IX*. SPIE LASE, San Francisco, California, United States, Saturday 7 February 2015 (SPIE 2015), 93510M
16. G. Bonamis, K. Mishchick, E. Audouard, C. Hönninger, E. Mottay, J. Lopez, I. Manek-Hönninger, *Journal of Laser Applications* (2019) doi:10.2351/1.5096087
17. P. Balling, J. Schou, *Reports on progress in physics*. Physical Society (Great Britain) (2013) doi:10.1088/0034-4885/76/3/036502
18. A. Reupert, M. Heck, S. Nolte, L. Wondraczek, *Adv. Optical Mater.* (2020) doi:10.1002/adom.202000633
19. L. Capuano, R. Pohl, R.M. Tiggelaar, J.W. Berenschot, J.G.E. Gardeniers, Römer, G. R. B. E., *Opt. Express* (2018) doi:10.1364/oe.26.029283
20. M. Macias-Montero, F. Muñoz, B. Sotillo, J. Del Hoyo, R. Ariza, P. Fernandez, J. Siegel, J. Solis, *Sci Rep* (2021) doi:10.1038/s41598-021-87765-z
21. C. Florian, D. Fischer, K. Freiberg, M. Duwe, M. Sahre, S. Schneider, A. Hertwig, J. Krüger, M. Rettenmayr, U. Beck, A. Undisz, J. Bonse, *Materials* (Basel, Switzerland) (2021) doi:10.3390/ma14071651
22. M. Garcia-Lechuga, N. Casquero, A. Wang, D. Grojo, J. Siegel, *Adv. Optical Mater.* (2021) doi:10.1002/adom.202100400
23. M. Garcia-Lechuga, O. Utéza, N. Sanner, D. Grojo, *Opt. Lett., OL* (2020) doi:10.1364/OL.382610
24. B. Guo, J. Sun, Y. Lu, L. Jiang, *Int. J. Extrem. Manuf.* (2019) doi:10.1088/2631-7990/ab3a24
25. *Ionization in the field of a strong electromagnetic wave* (1965)
26. P. Balling, in *Handbook of Laser Micro- and Nano-Engineering*, ed. by K. Sugioka (Springer International Publishing, Cham, 2020), p. 1
27. B. Rethfeld, *Physical review letters* (2004) doi:10.1103/PhysRevLett.92.187401
28. B.H. Christensen, P. Balling, *Phys. Rev. B* (2009) doi:10.1103/PhysRevB.79.155424
29. J.-L. Déziel, L.J. Dubé, C. Varin, *Phys. Rev. B* (2021) doi:10.1103/PhysRevB.104.045201
30. A. Vogel, J. Noack, G. Hüttman, G. Paltauf, *Appl. Phys. B* (2005) doi:10.1007/s00340-005-2036-6
31. B.K. Ridley, *Quantum Processes in Semiconductors* (Oxford University Press 2013)
32. J. Köhler, M. Wollenhaupt, T. Bayer, C. Sarpe, T. Baumert, *Opt. Express* (2011) doi:10.1364/OE.19.011638
33. N. Götte, T. Winkler, T. Meinl, T. Kusserow, B. Zielinski, C. Sarpe, A. Senftleben, H. Hillmer, T. Baumert, *Optica* (2016) doi:10.1364/OPTICA.3.000389
34. M. Wollenhaupt, A. Assion, T. Baumert, in *Springer Handbook of Lasers and Optics*, ed. by F. Träger (Springer New York, New York, NY, 2007), p. 937
35. C. Sarpe, J. Köhler, T. Winkler, M. Wollenhaupt, T. Baumert, *New J. Phys.* (2012) doi:10.1088/1367-2630/14/7/075021
36. M. Born, E. Wolf, A.B. Bhatia, P.C. Clemmow, D. Gabor, A.R. Stokes, A.M. Taylor, P.A. Wayman, W.L. Wilcock, *Principles of Optics* (Cambridge University Press 2013)
37. S. Guizard, A. Semerok, J. Gaudin, M. Hashida, P. Martin, F. Quéré, *Applied Surface Science* (2002) doi:10.1016/S0169-4332(01)00681-X
38. S.H. Møller, S.T. Andersen, P. Balling, *Phys. Rev. Research* (2020) doi:10.1103/PhysRevResearch.2.043010
39. V.V. Temnov, K. Sokolowski-Tinten, P. Zhou, D. von der Linde, *J. Opt. Soc. Am. B* (2006) doi:10.1364/JOSAB.23.001954
40. L. Lepetit, G. Chériaux, M. Joffe, *J. Opt. Soc. Am. B* (1995) doi:10.1364/JOSAB.12.002467
41. S.S. Mao, F. Quéré, S. Guizard, X. Mao, R.E. Russo, G. Petite, P. Martin, *Appl. Phys. A* (2004) doi:10.1007/s00339-004-2684-0
42. Dennis Dempsey, Garima C. Nagar, Christopher K. Renskers, Rostislav I. Grynko, James S. Sutherland, Bonggu Shim, *Opt. Lett.* (2020) doi:10.1364/OL.382645

43. M.A. van Dijk, M. Lippitz, D. Stolwijk, M. Orrit, *Opt. Express* (2007) doi:10.1364/oe.15.002273
44. T. Winkler, C. Sarpe, N. Jelzow, L. Lasse H., N. Götte, B. Zielinski, P. Balling, A. Senftleben, T. Baumert, *Applied Surface Science* (2016) doi:10.1016/j.apsusc.2015.11.182
45. T. Winkler, L. Haahr-Lillevang, C. Sarpe, B. Zielinski, N. Götte, A. Senftleben, P. Balling, T. Baumert, *Nature Phys* (2018) doi:10.1038/nphys4265
46. O. Marsalek, C.G. Elles, P.A. Pieniazek, E. Pluhařová, J. VandeVondele, S.E. Bradforth, P. Jungwirth, *The Journal of Chemical Physics* (2011) doi:10.1063/1.3664746
47. N. Linz, S. Freidank, X.-X. Liang, A. Vogel, *Phys. Rev. B* (2016) doi:10.1103/PhysRevB.94.024113
48. K.R. Siefertmann, Y. Liu, E. Lugovoy, O. Link, M. Faubel, U. Buck, B. Winter, B. Abel, *Nature chemistry* (2010) doi:10.1038/nchem.580
49. J. Hernandez-Rueda, N. Götte, J. Siegel, M. Soccio, B. Zielinski, C. Sarpe, M. Wollenhaupt, T.A. Ezquerria, T. Baumert, J. Solis, *ACS applied materials & interfaces* (2015) doi:10.1021/am508925m
50. S. Richter, F. Jia, M. Heinrich, S. Döring, U. Peschel, A. Tünnermann, S. Nolte, *Opt. Lett.*, OL (2012) doi:10.1364/OL.37.000482
51. A. Couairon, L. Sudrie, M. Franco, B. Prade, A. Mysyrowicz, *Phys. Rev. B* (2005) doi:10.1103/PhysRevB.71.125435
52. K. Liao, W. Wang, X. Mei, B. Liu, *Optics & Laser Technology* (2021) doi:10.1016/j.optlastec.2021.107201
53. V.P. Zhukov, S. Akturk, N.M. Bulgakova, *J. Opt. Soc. Am. B* (2019) doi:10.1364/JOSAB.36.001556
54. S. Courvoisier, N. Götte, B. Zielinski, T. Winkler, C. Sarpe, A. Senftleben, L. Bonacina, J.P. Wolf, T. Baumert, *APL Photonics* (2016) doi:10.1063/1.4948367
55. G. Campargue, B. Zielinski, S. Courvoisier, C. Sarpe, T. Winkler, A. Senftleben, L. Bonacina, T. Baumert, J.P. Wolf, *AIP Advances* (2018) doi:10.1063/1.5049678
56. B. Duckert, S. Vinkx, D. Braeken, M. Fauvart, *Journal of controlled release : official journal of the Controlled Release Society* (2021) doi:10.1016/j.jconrel.2020.10.068
57. M.P. Stewart, R. Langer, K.F. Jensen, *Chemical reviews* (2018) doi:10.1021/acs.chemrev.7b00678
58. G. GEY, *Cancer Res* **12**, 264 (1952)
59. R. Skloot, *The immortal life of Henrietta Lacks* (Crown Publ, New York, 2010)
60. B.P. Lucey, W.A. Nelson-Rees, G.M. Hutchins, *Archives of pathology & laboratory medicine* (2009) doi:10.5858/133.9.1463
61. T. Winkler, P. Balling, B. Zielinski, C. Sarpe, N. Jelzow, R. Ciobotea, A. Senftleben, T. Baumert, *Phys. Rev. Research* (2020) doi:10.1103/physrevresearch.2.023341